

Supplementary Information

Statistical dynamics of noise-like rectangle pulse fiber laser

*Yujia Li, Dongmei Huang, * Yihuan Shi, Chao Wang, and Feng Li*

Email: meihk.huang@polyu.edu.hk

By properly adjusting the polarization state and setting the pump power as 414 mW, the laser can operate in the NLRPL state. [Figure S1a](#) is the laser spectrum obtained by the OSA. The peak wavelength is 1558.7 nm, and the 3-dB spectral bandwidth is 2.04 nm. The pulse train in the time domain is shown in [Figure S1b](#). The repetition rate of the pulse train is 79.6 ns (coinciding with the fundamental frequency of 12.56 MHz), corresponding to the cavity length of about 16.3 m. The inset in [Figure S1b](#) is the clear envelope of the pulse with a rectangle-like shape. The duration of the rectangle-like pulse is about 591.7 ps. The radio-frequency spectrum is shown in [Figure S1c](#). The signal-to-noise ratio at the fundamental frequency of 12.56 MHz is about 58 dB, indicating that the cavity operates in a stable NLRPL state. As we know, the RF spectrum is the Fourier transform of the pulse train in the time domain. Because the pulse in the time domain has a rectangle-like envelope, the envelope of the RF spectrum should have a Sinc-function shape. Thus, we can observe an intensity change in the envelope of the RF spectrum. The dip on the RF spectrum is located at about 1.6 GHz, which is close to the reciprocal pulse duration of 591.7 ps. To experimentally confirm that the laser pulse belongs to the noise-like pulse, the laser's output is injected into the auto-correlator (FR-103HS, Femtochrome). The autocorrelation trace is shown in [Figure S1d](#), which has a very wide pedestal with a narrow coherence peak at the center. The narrow peak on the auto-correlation trace indicates that the rectangle laser pulse is indeed one kind of noise-like pulse but not the DSR pulse. According to the narrow peak on auto-correlation trace, we can expect that there are a bunch of disorganized pulses with stochastic durations, intervals, and peak powers located in the rectangle packet, which are difficult to be directly measured due to the limitation of the detection bandwidth.

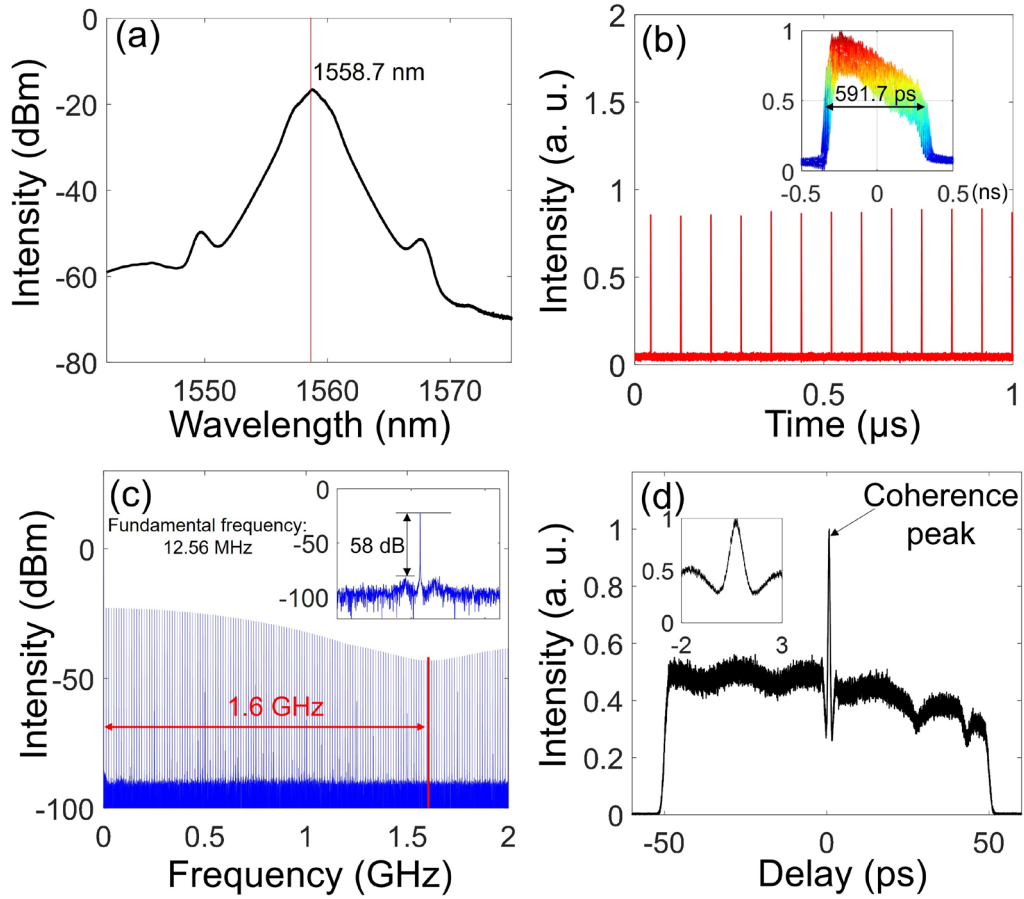


Figure S1. a) Laser spectrum with the pump power of 414 mW; b) pulse train of the NLRPL in the time domain, and the inset is the clear pulse envelope; c) RF spectrum of the output laser, and the inset is the zoom-in view at the fundamental frequency; d) auto-correlation trace of the NLRPL and the inset is the zoom-in view of the narrow central peak.

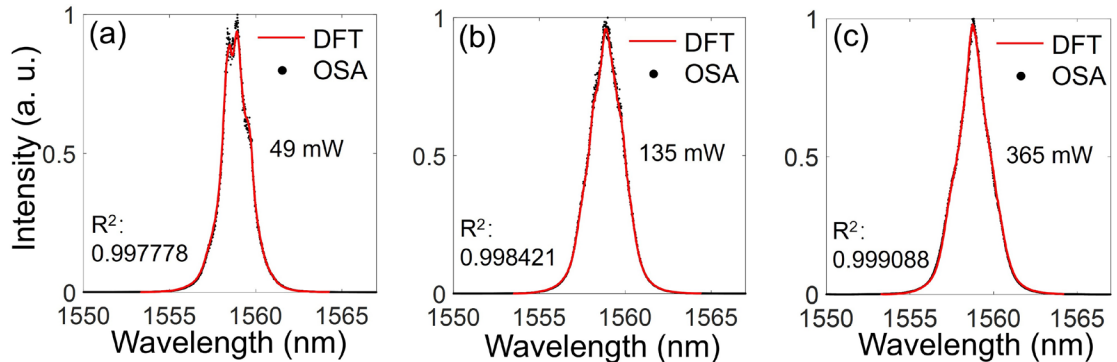


Figure S2. Comparison between the average spectra obtained by the DFT and OSA with the pump powers of a) 49 mW, b) 135 mW, and c) 365 mW.

The spectra of the NLRPL obtained by the DFT (red curve) and OSA (black points)

are compared as shown in [Figures S2a-S2c](#). The DFT spectra are the average curves of 251160 single-shot spectra. The two spectra in these figures are almost overlapped. Then, we utilize the coefficient of determination R^2 to estimate the fitting precision between the DFT- and OSA- based spectra. The expression of the R^2 can be expressed by:

$$R^2 = 1 - \frac{\sum_i (I_1(\lambda_i) - I_2(\lambda_i))^2}{\sum_i \left(I_1(\lambda_i) - \frac{1}{k} \sum_i I_1(\lambda_i) \right)^2}, \quad (\text{S1})$$

where k is the point number, and $I_1(\lambda_i)$ and $I_2(\lambda_i)$ are the spectral intensity at the wavelength component λ_i obtained by the OSA and DFT, respectively. R^2 is closer to 1, and the similarity between the DFT- and OSA-based spectra is higher. The coefficients of determination with the pump powers of 49 mW, 135 mW, and 365 mW reach 0.99778, 0.99841, and 0.999088, respectively, indicating that the DFT spectra coincide with the OSA spectra. Therefore, the DFT spectroscopy can precisely measure the spectra of the NLRPL.

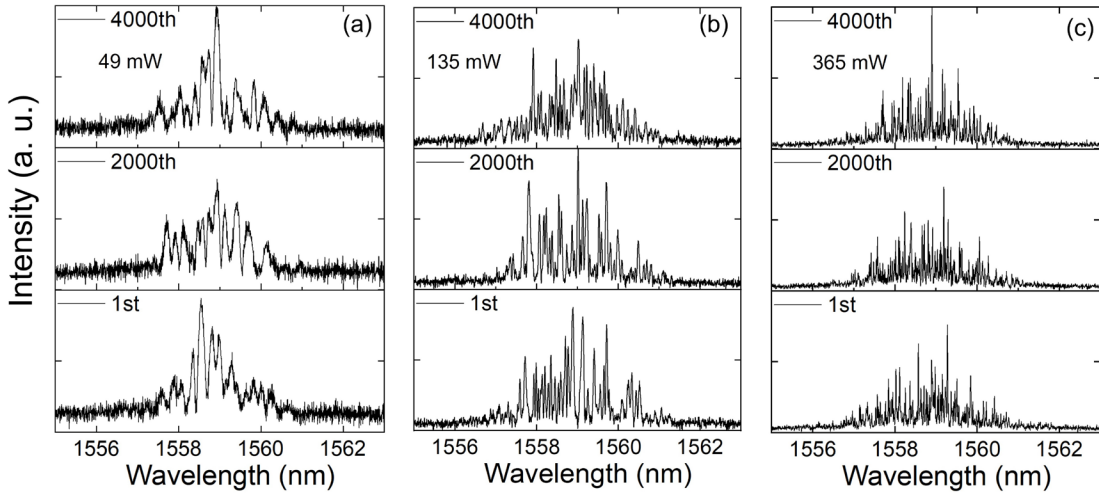


Figure S3. Single-shot spectra at the round trips of 1, 2000, and 4000 with the pump powers of a) 49 mW, b) 135 mW, and c) 365 mW.

Different from the single-shot spectra with high similarity to the average spectra in the stable coherent mode-locking state, most cluttered narrow pulses are randomly distributed on the single-shot spectra, as shown in [Figures S3a-S3c](#). With the enhancement of the pump power, the pulse width will be narrowed, and the spectral

pulse cluster becomes denser because of the enhanced self-phase modulation.

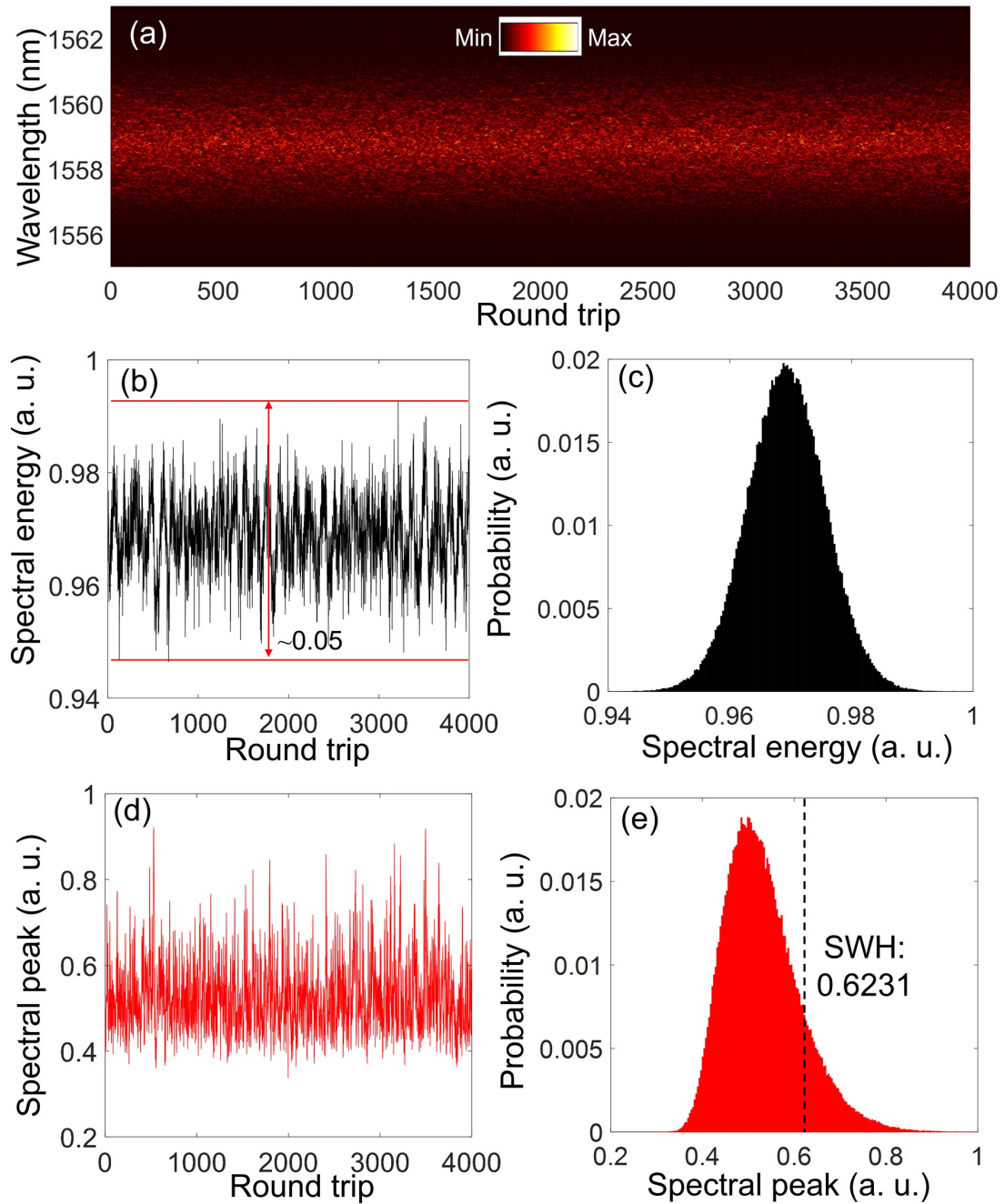


Figure S4. a) Single-shot spectral evolution of the NLRPL with the pump power of 414 mW; b) spectral energy evolution of the NLRPL; c) marginal probability distribution of the spectral energy; d) spectral peak evolution of the NLRPL; e) marginal probability distribution of the spectral peak.

The single-shot spectral evolution of the NLRPL with the pump power of 414 mW is shown in [Figure S4a](#). Although the spectral shape in the evolution process is entirely random, the spectral energy has just slight jitter within about 5% as shown in [Figure](#)

S4b. The probability distribution of the energy has a symmetrical Gaussian-like shape as shown in Figure S4c, which matches the vertical projection in Figure 3b. The relative jitter range of the spectral peak in the evolution process is much larger, as shown in Figure S4d, which corresponds to the higher noise level in Figure 3c. In Figure S4e, the marginal probability distribution has an asymmetrical shape with a tail right the black dashed line. The SWH is 0.6231, which indicates a small probability of generating a relatively large spectral peak and matches well with the horizontal projection of Figure 3b.

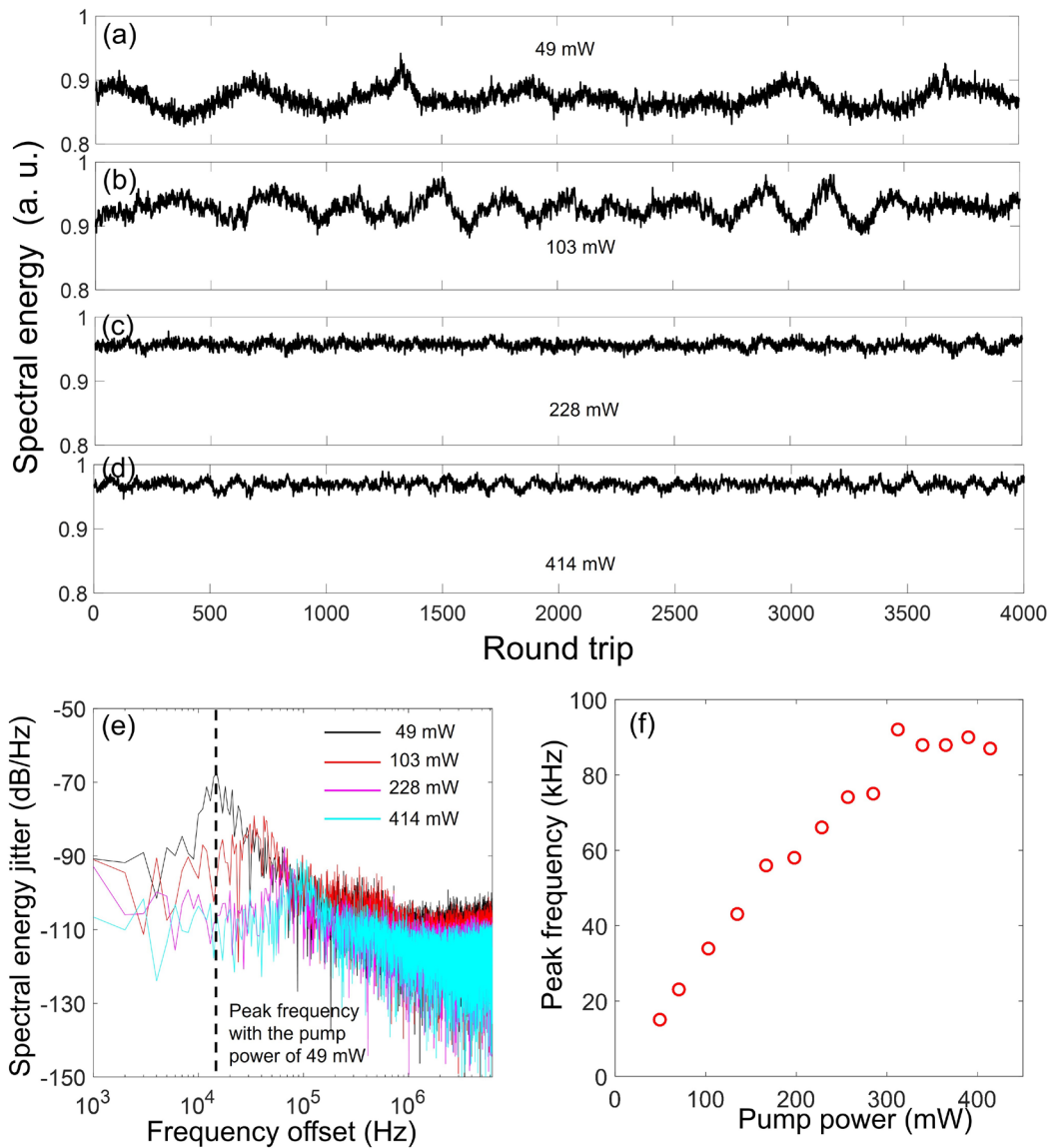


Figure S5. a)-d) Spectral energy evolutions and e) PSD of the spectral energy jitter with the pump powers of 49 mW, 103 mW, 228 mW, and 414 mW, respectively; f) Peak

frequencies under different pump powers.

The spectral energy evolutions with the pump power of 49 mW are shown in [Figure S5a](#). We can see that the energy jitter in the time domain has strong low-frequency fluctuations with an unfixed period of about several hundred round trips, leading to a wide noise peak aligned with the black dashed lines on the black curve in [Figure S5e](#). By increasing the pump power, the energy evolution will become more stable as shown in [Figures S5b-S5d](#). [Figure S5e](#) is obtained by calculating the power spectral density (PSD) of the spectral energy evolution, where the frequency resolution with 1 kHz is determined by the 1 ms time window of the Fourier transform. As a result, the noise peak has a red shift and is weakened, which can be observed in [Figure S5f](#). This phenomenon is similar to the breathing soliton in a mode-locking state [16]. The difference is that the breathing soliton has a fixed period, and the noise peak in the PSD is usually much narrower. However, due to the gain saturable effect, this changing tendency will disappear when the pump power is over 300 mW. Therefore, in the high pump power region, the peak frequency can hardly be increased even by increasing the pump power.

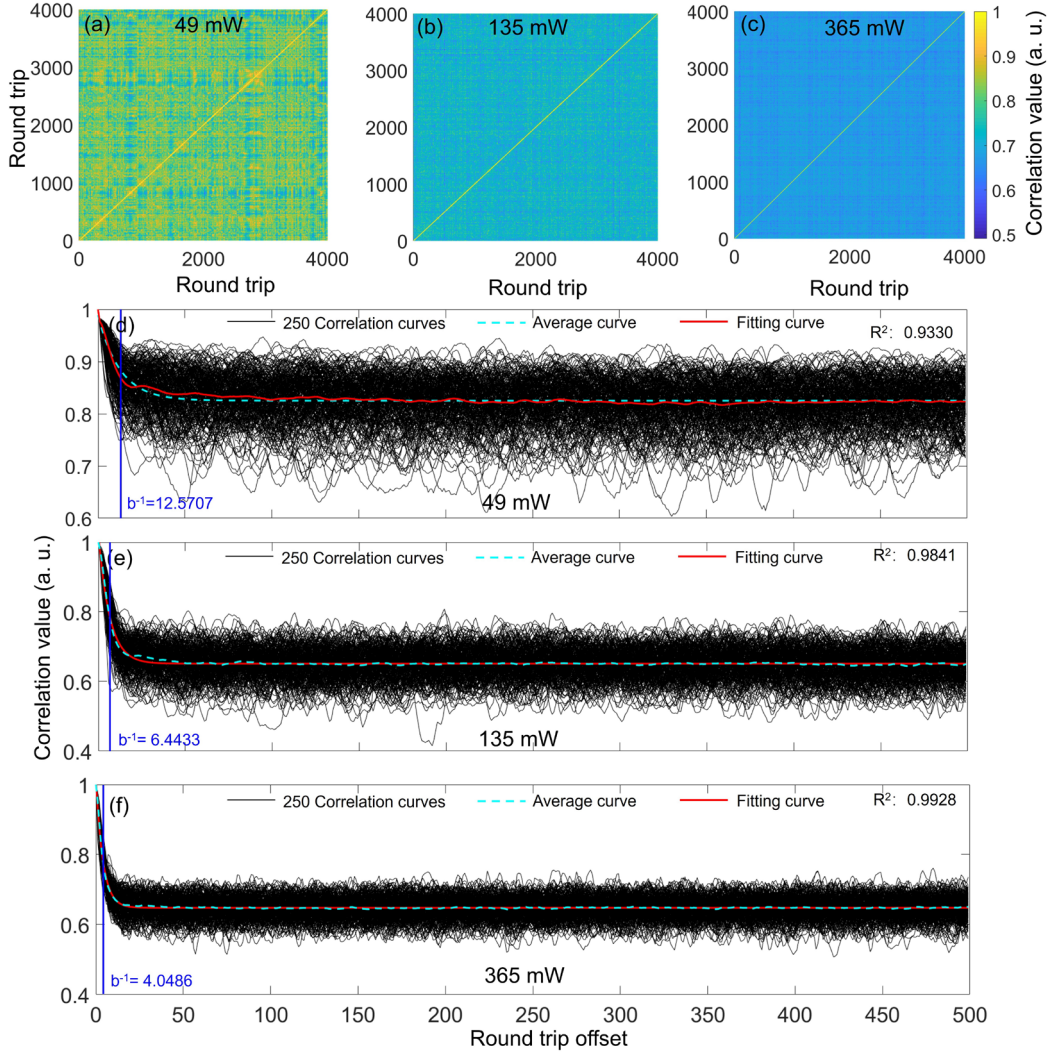


Figure S6. 2D map of the spectral correlation within 4000 round trips with the pump powers of a) 49 mW, b) 135 mW and c) 365 mW; spectral correlation curves within the round-trip-offset numbers from 0 to 500 and the corresponding fitting curves with the pump powers of d) 49 mW, e) 135 mW and f) 365 mW.

To further confirm the exponential tendencies of the spectral similarity, [Figure S6](#) gives more results corresponding to [Figure 5](#) in different pump powers. The 2D maps of the spectral correlations are shown in [Figure S6a-S6c](#). The correlation values on these maps have similar distributions as those in [Figure 5a](#). With the increment of the pump power, the region of high correlation values will become narrower. The spectral correlation curves within the round-trip-offset numbers from 0 to 500 and the corresponding fitting curves with the pump powers of 49 mW, 135 mW, and 365 mW are shown in [Figures S6d-S6f](#). Here, all the fitting curves satisfy the same fitting model:

$y=ae^{-bx}+c$, and the fitting R^2 are 0.9330, 0.9841 and 0.9928, respectively. The parameter b^{-1} can correctly reflect the decay speed with the offset number increased. The three values of b^{-1} are the 1st, 4th, and 12th data points in [Figure 5d](#). In [Figure 5b](#), to show the change of the correlation values more clearly, we just plotted the curve within the offset from 0 to 50.

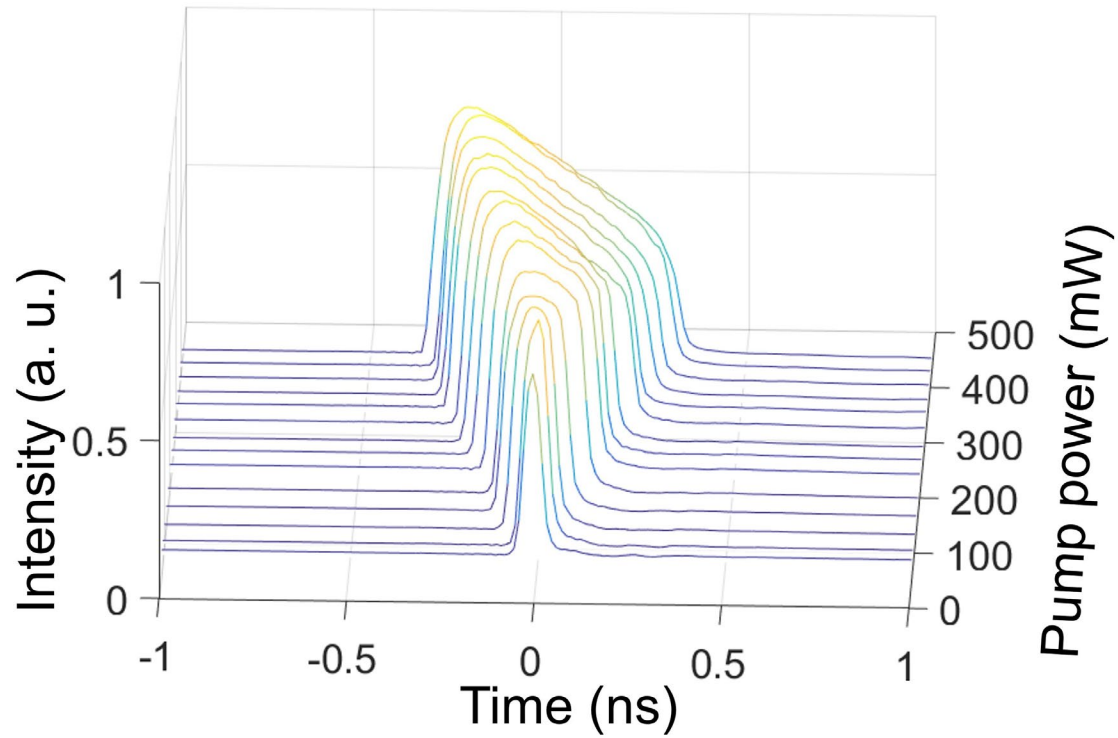


Figure S7. The evolution of the pulse in time domain with the pump power enhanced from 49 mW to 414 mW.

The curves in [Figure S7](#) are the average results of 12588 single-shot curves. The pulse width will be widened by increasing the pump power. The pulse width in [Figure 6e](#) is obtained by calculating the FWHM of the curves in [Figure S7](#).

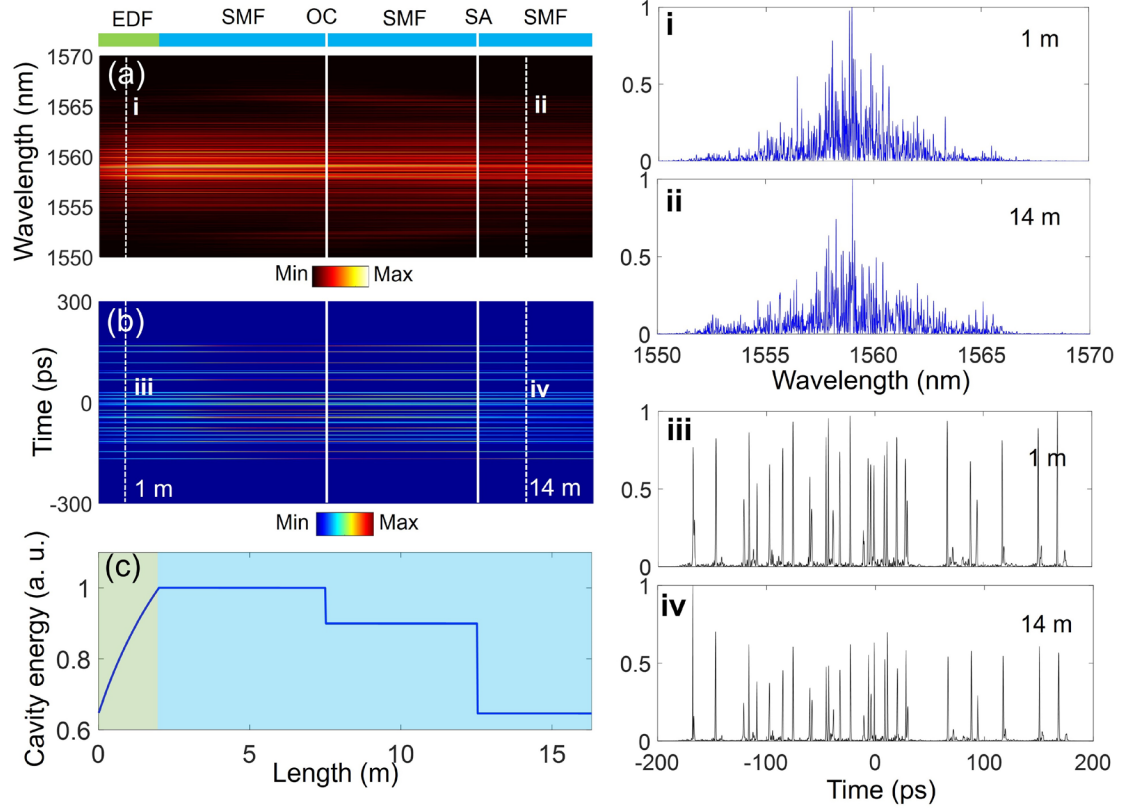


Figure S8. a)-c) The simulation results of inner-cavity evolutions of the spectrum, time-domain pulse intensity and pulse energy with the saturable pulse energy of 1.2 nJ; spectra (i, ii) and time-domain pulse intensities (iii, iv) corresponding to the vertical white lines in Figs. S8a-b.

The evolutions of the NLRPL's spectrum and pulse intensity in the time domain are shown in [Figures S8a-b](#). Due to the multi-pulse operation, the single-pulse energy is not very high. Therefore, the nonlinear effect induced by the EDF and SMF is relatively weak. Thus, the spectrum's shape and temporal pulse intensity just have slight changes after propagation with one round trip. They both represent the apparent multi-peak structures, as seen in [Figures S8i to S8iv](#). Although the change after the single round trip is small, it will be accumulated with the increment of the round-trip number, resulting in the random behaviors of the spectra and pulse envelope. The laser energy evolution is shown in [Figure S8c](#). The pulse energy is increased in the EDF, which can be balanced with the loss induced by the OC and SA (aligned with the white dashed lines in [Figures S8a-b](#)).

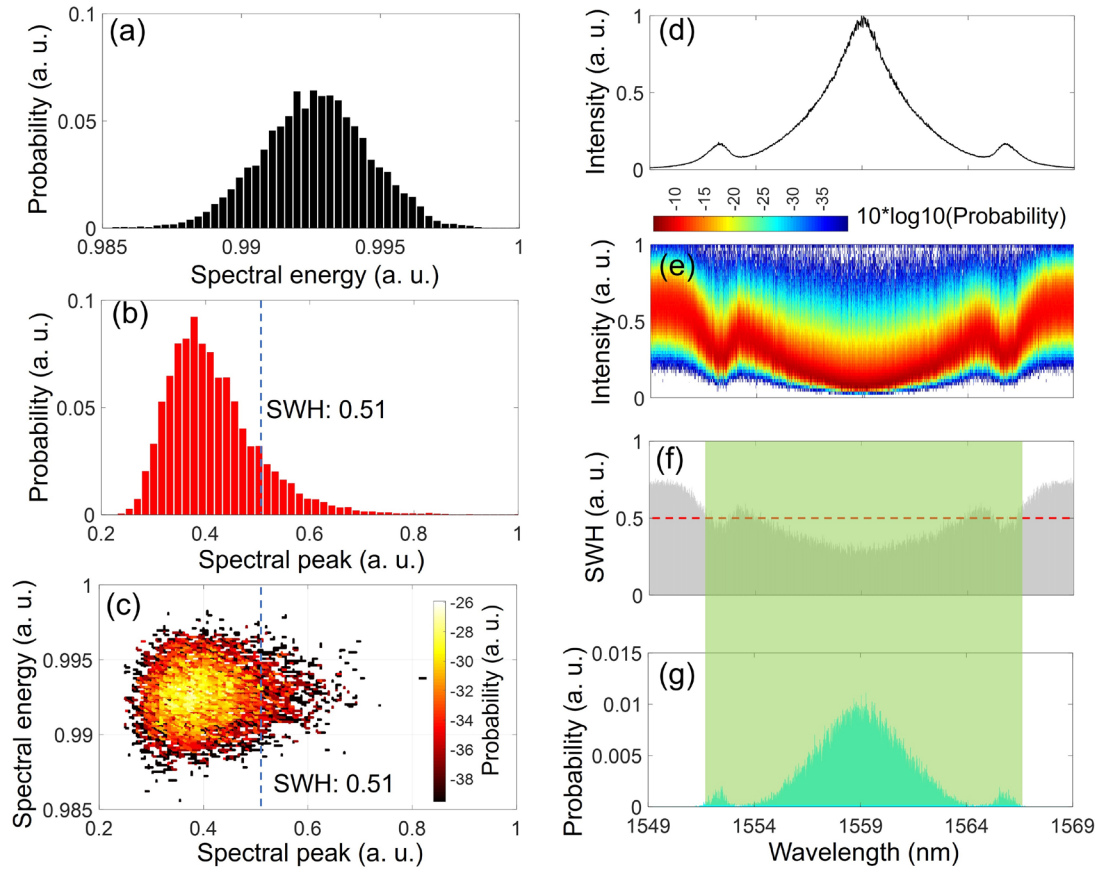


Figure S9. Simulated statistical properties of the NLRPL. a)-b) Marginal probability distributions of the spectral energy and spectral peak; c) joint probability distribution of the spectral energy and spectral peaks; d) average spectra of 9000 round trips; e) 2D map of the probability distribution of the spectral fluctuations; f) SHWs and g) probabilities of the extreme wave events at all spectral components.

The marginal probability distributions of the spectral energy and the peaks are shown in [Figures S9a](#) and [S9b](#). We also add the white noise to the simulated spectra because of the noise induced by PD and OSC. Similar to the results in [Figures S4c](#) and [S4e](#), the asymmetry of the probability distribution of the spectral energy is weaker than that of the spectral peak. The joint probability distribution of the spectral energy and spectral peaks is shown in [Figure S9c](#), where the SWH of the spectral peak is 0.51, indicating that no extreme wave events exist. This also coincides with the experimental results in [Figure S4e](#). [Figures S9d-S9g](#) are the simulation results corresponding to those in [Figures 4a-4d](#). The simulated average spectrum has obvious sidebands, which can also be experimentally observed in [Figure S1a](#). The sidebands in the simulation are just

stronger than that in the experiment. The proportion of the white noise with a Gaussian distribution will become larger with weaker light intensity. If we ignore the abnormal change of the intensity induced by the two sidebands with the wavelength far from the spectral center, spectral intensity at two sides is weaker than that of the spectral center. Since the Gaussian distribution is highly symmetrical, the symmetry of the probability distribution of the intensity fluctuation is stronger when the spectral component is far away from the spectral center. Thus, the obtained probability distribution should be commonly contributed by the light fluctuation with the inherently asymmetrical probability distribution and the detection noise of the PD and OSC with the symmetrical distribution. The SWH and probability of the extreme wave events at different spectral components are shown in Figures S9f and S9e. Similar to the experimental results in Figures 4c-4d, the SWH will increase with the asymmetry of the probability distribution weakened, which means that the probability of the extreme wave events will decrease. The region-covered green shadow can generate extreme wave events, whose probability at the spectral center is obviously larger than that at two sides.

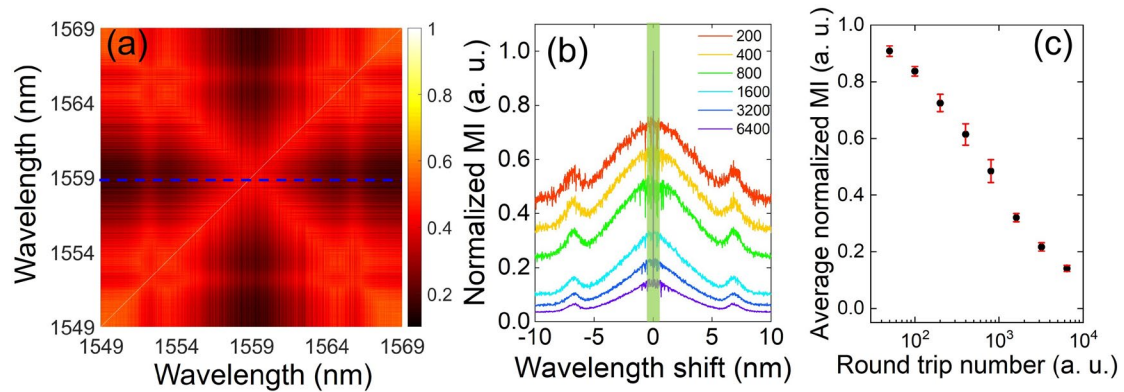


Figure S10. The MI results based on numerical simulation data. a) 2D map of the normalized MI of arbitrary two wavelengths within the range from 1550nm to 1567 nm, which is obtained by the spectral evolution with continuous 1000 round trips; b) normalized MI values on the blue 1D cutting line in Figure S10a with different total round trips; c) Average values of MI within the black shadow region with different total round trips.

The 2D MI map based on the simulated spectral evolution with 1000 round trips

are shown in Figure S10a, which is similar to the results in Figure 7d. Due to the influence of the stronger spectral sideband, there is a just slight difference in the MI map at the wavelength of the sidebands between the simulation and experimental results. As seen in Figure S10b, by increasing the total roundtrips, the value on the MI curve (corresponding to the blue dashed line in Figure S10a) decreases, which indicates a decreased mutual dependence between two spectral components within a longer statistical window. The change of the average normalized MI in the green region (± 0.5 nm) in Figure S10b coincides well with the experimental results in Figure 7f.

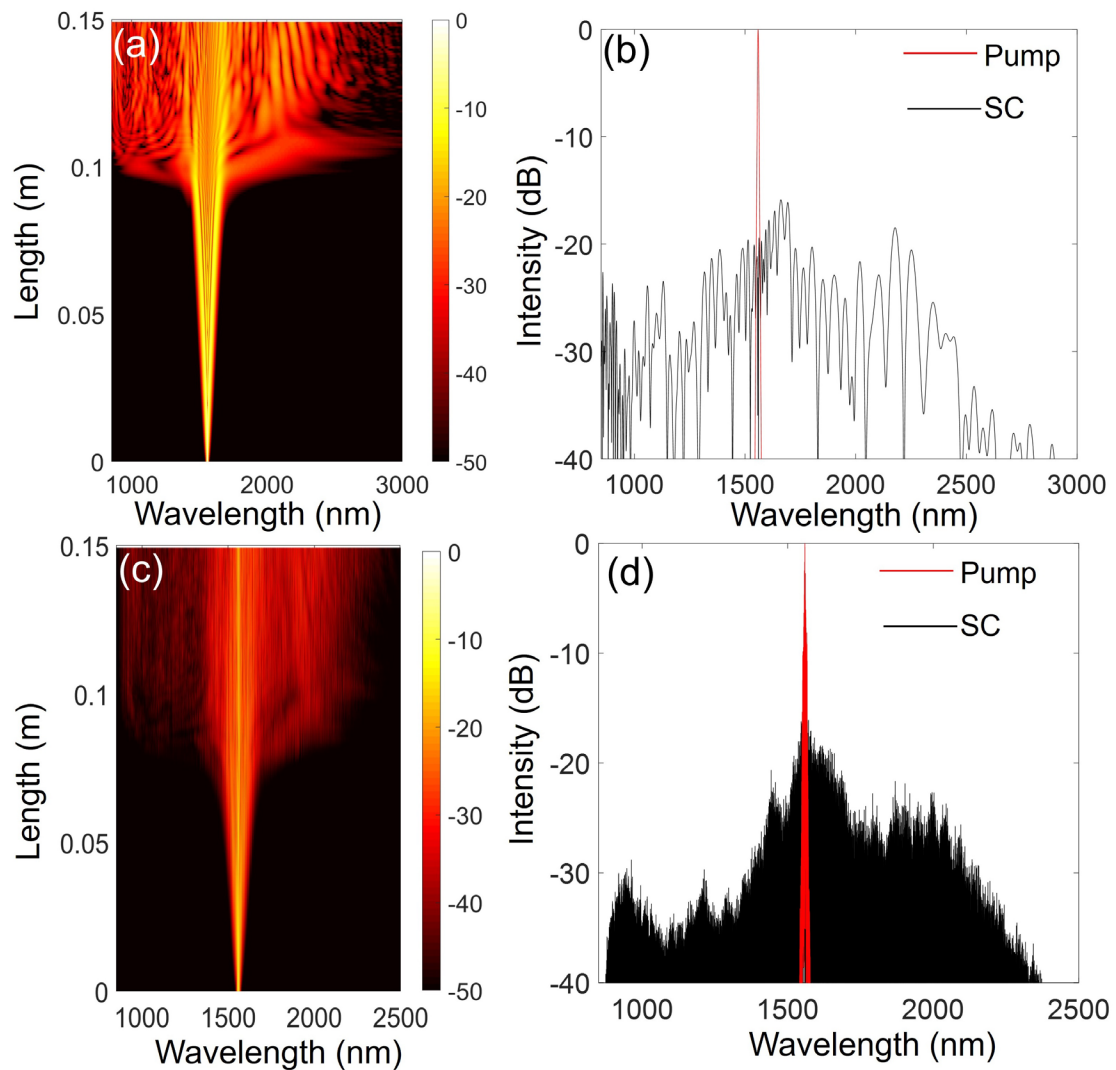


Figure S11 Numerical simulation results of the generation of the SC. a) 2D spectral evolution of the SC generation pumped by the sech^2 pulse; b) 1D spectra of the seed pump and the generated SC; c) 2D spectral evolution of the SC generation pumped by

the NLRPL; d) 1D spectra of the seed pump and the generated SC.

Here, we use the generalized nonlinear Schrödinger equation (GNLSE) to generate the SC. The equation of the model for the numerical simulation is written as [39]:

$$\frac{\partial A}{\partial z} + \frac{\alpha}{2} A - \sum_{k \geq 2} \frac{i^{k+1}}{k!} \beta_k \frac{\partial^k A}{\partial T^k} = i\gamma \left(1 + i\tau_{shock} \frac{\partial}{\partial T} \right) \left(A(z, T) \int_{-\infty}^{+\infty} R(T') \times |A(z, T - T')|^2 dT' \right), \quad (\text{S2})$$

where A is the complex amplitude of the electrical field, α is the propagation loss of the pulse, β is the dispersive coefficient, τ_{shock} is the Raman response time scale. k is the order of the dispersion, and γ is the nonlinear coefficient. $R(t)$ is the Raman response function, which is expressed as

$$\begin{aligned} R(t) &= (1 - f_R) \delta(t) + f_R h_R(t), \\ h_R(t) &= (\tau_1^{-2} + \tau_2^{-2}) \tau_1 \exp(-t / \tau_2) \sin(t / \tau_1) \end{aligned} \quad (\text{S3})$$

where f_R is the contribution of the Raman effect. The parameters for the numerical simulation are shown in Tab. S1

Parameter	Value	Parameter	Value
β_2	$-11.830 \text{ ps}^2/\text{km}$	γ	0.05 /m/W
β_3	$8.1038 \times 10^{-2} \text{ ps}^3/\text{km}$	τ_{shock}	0.56 fs
β_4	$-9.5205 \times 10^{-5} \text{ ps}^4/\text{km}$	α	0
β_5	$2.0737 \times 10^{-7} \text{ ps}^5/\text{km}$	f_R	0.18
β_6	$-5.3943 \times 10^{-10} \text{ ps}^6/\text{km}$	τ_1	12.2 fs
β_7	$1.3486 \times 10^{-12} \text{ ps}^7/\text{km}$	τ_2	32 fs
β_8	$-2.5495 \times 10^{-15} \text{ ps}^8/\text{km}$		
β_9	$3.0524 \times 10^{-18} \text{ ps}^9/\text{km}$		
β_{10}	$-1.7140 \times 10^{-21} \text{ ps}^{10}/\text{km}$		

Table S1 The parameters used for the numerical simulation.

Firstly, we use the standard sech^2 pulse as the seed pump to generate the SC. The spectral evolution dynamics of the pulse are shown in [Figure S11a](#), and the length of the propagation medium is 0.15 m. The spectrum is obviously broadened in the medium

due to the self-phase modulation. The 1D spectra of the initial pump pulse and the generated SC are shown in [Figure S11b](#). The spectral range of the SC can cover over 1000 nm. In the broadening process, the spectral shape is deteriorated, and the spectrum of the SC is not flattened, which is disadvantageous in the particle applications. As a comparison, we use the complex amplitude of the simulated NLPPR as the initial condition to generate the SC, and the 2D spectral evolution of the spectral broadening process is shown in [Figure S11c](#). The corresponding 1D spectra of the NLRPL and the SC are shown in [Figure S11d](#). Different from the pure sech^2 pulse pump, there are random interval and relative phase between the narrow pulses in the pulse cluster of the NLRPL, and the intensity of the narrow pulses are also different. Due to the complex interaction between random multiple pulses of the NLRPL, the shape of the spectrum of the generated SC has disorganized structure.